Applied Physics Letters

Loss channels affecting lithium niobate phononic crystal resonators at cryogenic temperature

Cite as: Appl. Phys. Lett. **118**, 123501 (2021); https://doi.org/10.1063/5.0034909
Submitted: 23 October 2020 • Accepted: 03 March 2021 • Published Online: 22 March 2021

E. Alex Wollack, Agnetta Y. Cleland, Patricio Arrangoiz-Arriola, et al.

Applied Physics Letters ARTICLE scitation.org/journal/apl

Loss channels affecting lithium niobate phononic crystal resonators at cryogenic temperature

Cite as: Appl. Phys. Lett. **118**, 123501 (2021); doi: 10.1063/5.0034909
Submitted: 23 October 2020 · Accepted: 3 March 2021 ·
Published Online: 22 March 2021

E. Alex Wollack,[a] Agnetta Y. Cleland, Patricio Arrangoiz-Arriola,[b] Timothy P. McKenna, Rachel G. Gruenke, Rishi N. Patel, Wentao Jiang, Christopher J. Sarabalis, and Amir H. Safavi-Naeini[a]

AFFILIATIONS

Department of Applied Physics and Ginzton Laboratory, Stanford University 348 Via Pueblo Mall, Stanford, California 94305, USA

[a]**Authors to whom correspondence should be addressed:** ewollack@stanford.edu and safavi@stanford.edu
[b]**Present address:** AWS Center for Quantum Computing, Pasadena, California, USA.

ABSTRACT

We investigate the performance of microwave-frequency phononic crystal resonators fabricated on thin-film lithium niobate for integration with superconducting quantum circuits. For different design geometries at millikelvin temperatures, we achieve mechanical internal quality factors Q_i above 10^5–10^6 at high microwave drive power, corresponding to 5×10^6 phonons inside the resonator. By sweeping the defect size of resonators with identical mirror cell designs, we are able to indirectly observe signatures of the complete phononic bandgap via the resonators' internal quality factors. Examination of quality factors' temperature dependence shows how superconducting and two-level system (TLS) loss channels impact device performance. Finally, we observe an anomalous low-temperature frequency shift consistent with resonant TLS decay and find that the material choice can help to mitigate these losses.

The field of circuit quantum acousto-dynamics (cQAD) has recently gained traction as a viable way to achieve quantum control of mechanical resonators via piezoelectric coupling to a superconducting qubit.[1–8] Manipulation and measurement of the quantum states of bulk acoustic wave (BAWs),[3,4] surface acoustic wave (SAWs),[5,7] and phononic crystal[6] resonators have demonstrated the capability of these hybrid systems. One of the primary motivations for integrating acoustic resonators with superconducting qubits is the advantages that mechanical systems can offer for scaling qubit architectures[9,10] that utilize bosonic systems to store quantum information. Not only have mechanical resonators been shown to have lifetimes comparable to[11] and exceeding[12] conventional superconducting resonators,[13,14] but they can also be extremely compact due to the slow speed of sound in most materials. Combined with proposals utilizing mechanical resonators as quantum memories,[15,16] these systems offer a path toward increasing computational complexity of existing superconducting qubit processors.

Toward achieving these goals, phononic crystal resonators offer some unique advantages over other cQAD platforms. The complete phononic bandgap induced by the crystal's periodic patterning not only tightly localizes mechanical motion but also offers protection against spurious acoustic radiation of the superconducting circuit. In contrast to approaches based on bulk acoustic or surface acoustic waves,[17] the phononic bandgap suppresses scattering loss due to inevitable fabrication disorder, such as surface or electrode roughness or isotopic impurities.[18] It is also straightforward to precisely engineer the frequency and coupling strength of these resonators, a key requirement to be able to perform quantum operations without crosstalk in certain proposals.[16] Despite these advantages, recent demonstrations of coupling phononic crystal resonators to qubits have been limited by the coherence times of the mechanical system,[6] motivating the need to better understand these devices' performance and limitations.

The nanomechanical resonators explored in this study are one-dimensional phononic crystal resonators made from thin-film lithium niobate (LN), each consisting of a defect site embedded in an acoustic shield [Figs. 1(a)–1(d)].[2,6,19] The periodic patterning of the shield opens a complete phononic bandgap for all acoustic polarizations in the 1.65–2.1 GHz range, confining mechanical motion to the defect and thereby minimizing clamping losses. Due to lithium niobate's strong piezoelectricity, aluminum electrodes placed on or near the defect are able to achieve large electromechanical coupling to the fundamental shear mode of the defect site. By sweeping the size of the defect width from 0.5 to 2.5 μm, a large array of devices is densely frequency multiplexed from 1.5 to 3.0 GHz to cover frequencies both inside and outside of the phononic bandgap. In studying this collection of devices, our goal is to understand the effect of the phononic

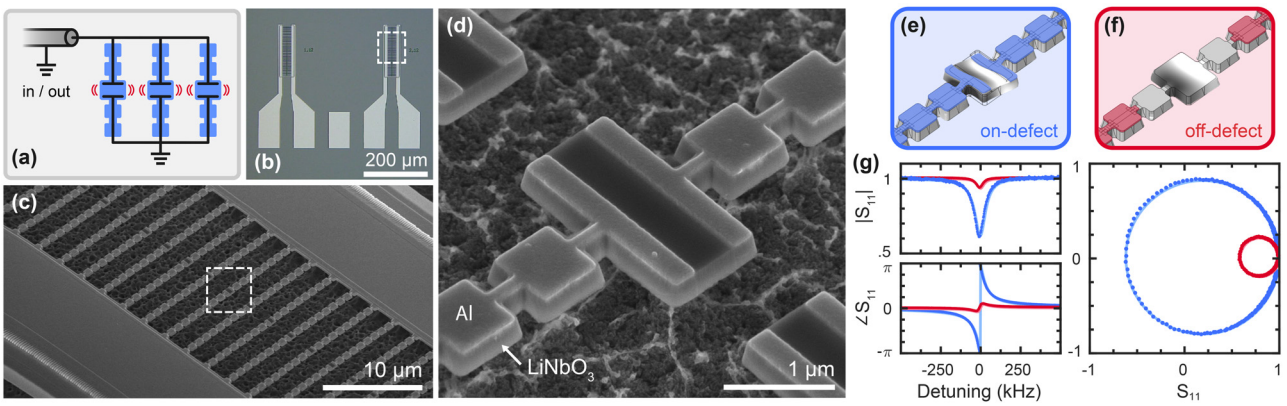

FIG. 1. Device overview. (a) Schematic of the device, with phononic crystal resonators inserted at the end of a microwave transmission line and measured on reflection. (b) Optical micrograph of two neighboring devices, each with 40 mechanical resonators placed between aluminum contact pads. (c) Scanning-electron micrograph (SEM) of the suspended mechanical resonators. (d) SEM image of the phononic crystal defect site showing aluminum electrodes on top of lithium niobate. [(e) and (f)] Finite-element simulations of the defect site's strongly coupled mode, showing the structure's localized mechanical deformation and associated electrostatic potential (grayscale). The aluminum electrodes (shaded blue/red) extend onto the defect site for the on-defect designs (e) in contrast to the off-defect designs (f), where the electrodes are one unit cell removed from the mechanically active defect region. (g) Normalized reflection S_{11} measurements for on-defect (blue) and off-defect (red) resonators, with fits to Eq. (1) (solid lines). The magnitude $|S_{11}|$ and phase $\angle S_{11}$ are plotted vs the detuning relative to the resonant frequency $\omega_r/2\pi \simeq 2.0$ GHz. S_{11} is also plotted in the complex plane (horizontal axis: real part; vertical axis: imaginary part). The response of the off-defect device is enlarged by a factor of ∼10 for visual clarity.

bandgap, electrodes, and material properties on the mechanical quality factors of phononic crystal resonators.

We fabricate devices from thin-film, MgO-doped lithium niobate on silicon, where an etch process is used to define the phononic crystals in the LN. Subsequent lithographic masks add the aluminum electrodes and contact pads, after which the resonators are suspended by isotropically etching the silicon substrate. For material comparison, we also fabricate nominally identical devices from congruent-LN, which is known to have crystalline defects due to missing lithium atoms. A detailed fabrication process is presented in the supplementary material, with Figs. 1(b)–1(d) showing the final fabricated resonators. Owing to their compact and highly parallelizable nature, we are able to fabricate 40 resonators per device in an $\sim 50 \times 200\ \mu m^2$ footprint. In order to better understand the effect of the aluminum electrodes on resonator coherence times, we design and fabricate resonators with two different electrode configurations: on-defect [Fig. 1(e)] and off-defect [Fig. 1(f)]. The close proximity of the on-defect electrodes allows for over an order of magnitude enhancement in electromechanical coupling compared to the off-defect designs, coming at the cost of additional mechanical losses from the aluminum.

Inserting these devices at the end of a 50 Ω microwave transmission line allows for extraction of device properties via microwave reflection measurements, with representative results shown in Fig. 1(g). We fit each resonator's scattering parameter S_{11} using the diameter correction method,[20]

$$S_{11}(\omega) = 1 - e^{i\phi}\frac{Q}{Q_e}\frac{2}{1 + 2iQ\dfrac{\omega - \omega_r}{\omega_r}}, \tag{1}$$

where ω_r is the resonant frequency and the total quality factor $Q = (Q_e^{-1} + Q_i^{-1})^{-1}$ is composed of the coupling Q_e and internal Q_i quality factors. Here, $e^{i\phi}$ accounts for any circuit asymmetry caused by an impedance mismatch in the resonator's microwave environment and avoids overestimating Q_i for large asymmetries.[20,21] All microwave measurements are performed at millikelvin temperatures in a dilution refrigerator, with standard shielding, thermalization, and filtering for superconducting resonators.[21]

Upon cooling the 40-resonator devices, we initially search for signatures of the phononic bandgap by classifying and characterizing the designed modes in the frequency range spanning $1.5 - 3.0$ GHz (see the supplementary material for details). All resonators have the same mirror cell design with the simulated band structure shown in Fig. 2(a), while the defect size is swept to place resonant frequencies both in and out of the full phononic bandgap. In Fig. 2(b), measured internal quality factors Q_i show over an order of magnitude enhancement for resonators inside the simulated bandgap relative to those outside. These measurements are performed at 800 mK with high microwave power (5×10^6 intra-cavity phonons) in order to maximize Q_i and saturate any two-level systems loss channels. Despite being outside of the bandgap, modes still can exist in the ∼2.1–2.8 GHz range because the corresponding mirror cell band has opposite symmetry to the defect's eigenmode; the magnitude of this symmetry-dependent protection is likely limited by any physical asymmetry in the fabricated device.[22] Above 2.8 GHz, the phononic band structure is both denser and contains bands of the same symmetry as the defect mode, causing these higher frequency modes to have significant leakage.

After determining the location of the phononic bandgap, we explore the properties of these high-Q_i modes for integration with superconducting quantum devices. Since the phononic bandgap eliminates all scattering losses, the Q_i of these devices must be limited by other physical processes. We are primarily interested in how these devices operate when cooled to the millikelvin temperatures where operation in the quantum regime is possible. At such low temperatures, nonlinear processes such as Akhiezer, Landau-Rumer, and thermoelastic damping are greatly diminished,[23] leading us to consider the

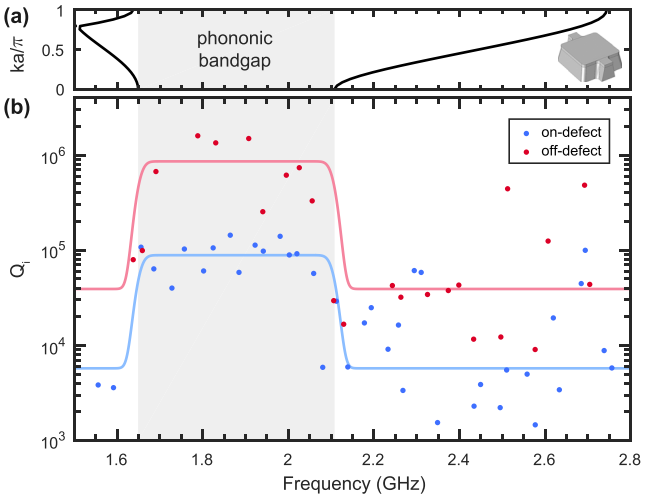

FIG. 2. Signatures of the phononic bandgap. (a) Simulated band diagram for the mirror unit cell (pictured, right) forming the tethers of the defect site, with the full phononic bandgap from 1.65 to 2.1 GHz shaded (gray). (b) Internal quality factor Q_i as a function of resonant frequency for the on-defect (blue) and off-defect (red) 40-resonator MgO-doped devices at 800 mK. By design, the resonant frequencies are swept across the simulated location of the phononic bandgap. The solid lines are guides to the eye, connecting the average Q_i inside the simulated bandgap to the median Q_i outside of the bandgap and demonstrating over an order of magnitude Q_i enhancement in the protected region. The skewed distribution in Q_i outside the bandgap makes the median a better indicator of typical device performance.

resonators' two primary loss channels: (i) two-level system (TLS) defects coupled to the mechanical resonance and (ii) Ohmic and quasiparticle losses due to currents induced in the electrode metal via the piezoelectric effect.

TLS defects are typically associated with two nearly degenerate low-energy configurations of an amorphous material,[24] and can couple to the strain or electric fields generated by excitation of a piezoelectric resonator. At single-phonon occupancy levels and millikelvin temperatures, TLSs are no longer saturated, allowing them to cause dissipation and decoherence in coupled devices. Because these material losses are thought to dominate qubit and resonator lifetimes, TLSs have been studied extensively in superconducting resonators,[21,25] as well as low- ($\lesssim 100$ MHz)[26–29] and high- ($\gtrsim 1$ GHz)[12,30–32] frequency mechanical resonators.

Generically, TLSs affect the resonator via resonant and relaxation processes, with the latter being strongly dependent on the dimensionality d of the system.[12,29,33] In resonant processes, the TLS serves as an acoustic bath which the resonator can decay into, resulting in a temperature- and power-dependent contribution to the resonator loss,[24,25,33]

$$Q_{i,\mathrm{res}}^{-1} = F\delta_{\mathrm{TLS}}^{0}\frac{\tanh\left(\frac{\hbar\omega_r}{2k_BT}\right)}{\sqrt{1+\langle n\rangle/n_c}}. \quad (2)$$

Here, $\delta_{\mathrm{TLS}}^{0}$ is the intrinsic TLS loss tangent at zero temperature, F is the filling fraction of the TLS in the host material, $\langle n\rangle$ is the average phonon number in the resonator, and n_c is the critical phonon number for TLS saturation. Resonant TLS absorption does not depend on the system dimensionality – up to a small numerical correction[33]—and so the reduction in $Q_{i,\mathrm{res}}$ at sufficiently low temperature should be the same in both superconducting and d-dimensional mechanical resonators.

In contrast, relaxation absorption occurs due an interaction with the off-resonant TLS, in which the oscillatory motion of the resonator causes local strain and electric field variations that perturb the TLS environment and modulate their energy levels. This modulation periodically displaces the TLS from thermal equilibrium, with their subsequent relaxation back to equilibrium effectively damping the resonator. This process is strongly dependent on the dimensionality d of the system, set by the device geometry, mode dispersion, and phonon bath density of states seen by the thermally active TLS with frequencies $\omega_{\mathrm{TLS}} \simeq k_BT/\hbar$. When limited by relaxation processes, the effective system dimension can be probed via the temperature dependence of the relaxation loss channel,[12,29,33] $Q_{i,\mathrm{rel}}^{-1} \sim T^d$ (see the supplementary material for further discussion).

In order to identify loss channels in the phononic crystal resonators, we extract the internal loss Q_i from microwave reflection measurements at a variety of fridge temperatures (Fig. 3). For on-defect designs, we find that normal-metal losses in the aluminum dominate until the onset of superconductivity at $T_c \simeq 1.2$ K. These normal-metal losses can be explained by the variation in electric potential on the surface of the defect site, where excitation of the fundamental shear mode piezoelectrically induces a gradient in the potential *within* each electrode. The resulting internal currents would then cause Ohmic losses associated with the excitation of the resonance, not simply insertion loss from the leads. At intermediate temperatures below T_c, Q_i is limited by thermal population of quasiparticles in the electrodes, described by the Mattis-Bardeen formulas for AC conductivity of a BCS superconductor.[34–36] With further reduction in temperature, resonant TLS losses outweigh superconducting loss channels, as evidenced by the absence of the frequency blueshift predicted by

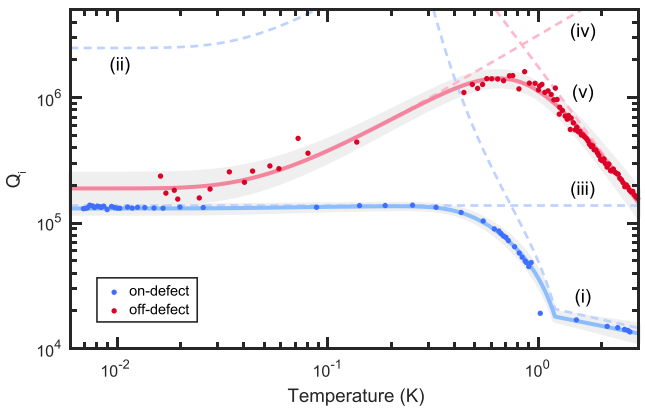

FIG. 3. Quality factor measurements. Internal quality factor Q_i vs fridge temperature for an on-defect (blue) and an off-defect (red) MgO-doped device with resonant frequency $\omega_r/2\pi \simeq 2.0$ GHz. The on-defect device is fit to (i) Mattis–Bardeen theory with (ii) resonant TLS decay at low temperatures and (iii) temperature-independent mechanical loss from the aluminum. Due to the absence of superconducting electrodes for the off-defect device, we fit to a TLS model, which includes both (iv) resonant decay and (v) relaxation damping processes. Solid lines denote fits to each device's total model, with gray shaded regions corresponding to 95% confidence intervals for the fits. We remark that on- and off-defect measurements were performed at high power, $\langle n\rangle \simeq 5\times10^6$ and 1.3×10^4, respectively, leading to a large power-enhancement in $Q_{i,\mathrm{res}}$ at low temperature.

Mattis-Bardeen theory in Fig. 4(a). However, we suspect the grain-boundary mechanical losses of the polycrystalline aluminum electrodes[37] impose an approximately temperature-independent limit on Q_i, diminishing the visibility of resonant TLS loss $Q_{i,\mathrm{res}}^{-1}(T)$ for $T \lesssim \hbar\omega_r/2k_B$ in Fig. 3.

For off-defect designs, we see markedly different behavior due to the off-defect resonator's electrodes being placed far from the mechanically active region. This means that aluminum's normal-metal, quasiparticle, and mechanical loss channels should be negligible for all temperatures, in agreement with the absence of any feature in $Q_i(T)$ near the T_c of aluminum and the two orders of magnitude higher $Q_i(T_c)$ than on-defect devices. Instead, we find TLS relaxation absorption dominates for temperatures above $T \gtrsim 1$ K, where $Q_{i,\mathrm{rel}}^{-1} \sim T^d$ scales as the effective phonon bath dimension, $d = 2.28 \pm 0.06$. Below $T \simeq 300$ mK, we estimate the wavelength of thermal phonons $\lambda_{\mathrm{th}} \simeq 1\ \mu$m should be larger than both the LN thickness (250 nm) and most feature sizes of the device, leading to a further reduction in the effective dimension. However, the resonant TLS already contributes significantly to the device's Q_i by this temperature, preventing observation of this geometry- and temperature-dependent damping for the relaxation TLS in a mesoscopic device.[33] Detailed analysis of both the on- and off-defect models for $Q_i(T)$ can be found in the supplementary material.

While sweeping the temperature, we also look for signatures of the TLS by monitoring the resonant frequency of the mechanical mode [Fig. 4(a)]. Due to interactions with the resonant TLS, the relative frequency shift $\Delta\omega_r/\omega_r$ of the resonator is described by[24,25]

$$\frac{\Delta\omega_r}{\omega_r} = \frac{F\delta_{\mathrm{TLS}}^0}{\pi}\left[\mathrm{Re}\left\{\Psi\left(\frac{1}{2}+\frac{\hbar\omega_r}{2\pi i k_B T}\right)\right\} - \ln\frac{\hbar\omega_r}{2\pi k_B T}\right], \quad (3)$$

where Ψ is the complex digamma function. This anomalous frequency redshift with decreasing temperature stands in contrast to the blueshifts associated with stiffening of the material [Fig. 4(b)] or the suppression of thermal quasiparticles in Mattis-Bardeen theory. Fits of $\Delta\omega_r/\omega_r$ in Fig. 4(a) to Eq. (3) provide an indirect method to extract the average total TLS loss $F\delta_{\mathrm{TLS}}^0$ with high microwave probe power. In this measurement, far-detuned TLS still contribute significantly to the resonator's frequency shift at low temperature, thereby giving a spectrally averaged value of TLS loss.[38] For both on- and off-defect devices made from congruent-LN, we report an average total TLS loss $F\delta_{\mathrm{TLS}}^0 = (1.28 \pm 0.09) \times 10^{-4}$, while devices on MgO-doped LN achieve lower loss, $F\delta_{\mathrm{TLS}}^0 = (5.5 \pm 0.1) \times 10^{-5}$. We note that the congruent-LN measurements include resonances both in and out of the phononic bandgap and are consistent across several fabrication batches and cooldowns. In Fig. 4(c), we plot $F\delta_{\mathrm{TLS}}^0$ vs the defect width to determine if TLS loss scales with geometry, as was found for coplanar waveguide resonators.[25] Both due to the narrow range of defect sizes and ambiguity in the relative contributions of electric- and strain-coupled TLSs to the filling fraction F in a piezoelectric material, we are unable to differentiate between a bulk or surface TLS distribution. However, the significant decrease in TLS loss for MgO-doped LN suggests that the TLS loss may be mitigated through better material choices. For example, LN is known to have crystal defects due to missing lithium atoms, and these vacancies can be filled via re-lithiation or MgO-doping.

In summary, we have demonstrated phononic crystal resonators with internal quality factors $Q_i \simeq 10^5 - 10^6$ at high drive powers, with 5×10^6 phonons in the resonator. Detection of the fundamental phononic bandgap from 1.65 to 2.1 GHz via internal quality factor Q_i shows over an order of magnitude enhancement in Q_i for modes inside the phononic bandgap. Through the measurement of Q_i vs temperature, we are able to demonstrate how normal-metal, quasiparticle, and TLS loss channels affect device performance. The best observed average total TLS loss $F\delta_{\mathrm{TLS}}^0 = (5.5 \pm 0.1) \times 10^{-5}$ for devices made from MgO-doped lithium niobate implies a single phonon $Q_i \simeq 2 \times 10^4$ is achievable with current generation devices. Understanding the origin of the TLS in lithium niobate remains an outstanding challenge, requiring further advances in materials and fabrication.

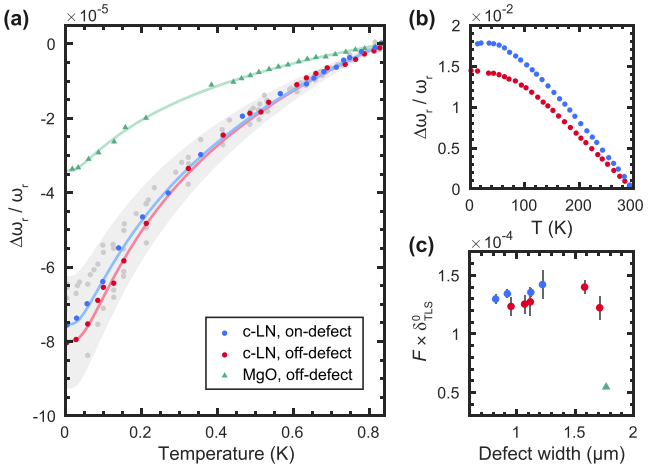

FIG. 4. Anomalous low-temperature frequency shift. (a) Fractional shift in resonance frequency $\Delta\omega_r/\omega_r$ vs temperature, referenced to the resonator frequency at 800 mK. Devices fabricated from congruent-LN (●) show dramatically different behavior than devices made from MgO-doped LN (▲). Solid lines are fits to a TLS model [Eq. (3)] with a small incident thermal bath. For clarity, data from additional c-LN devices are shown as gray circles, and the shaded gray region indicates 95% bounds on the c-LN devices' TLS loss. (b) Fractional frequency shift referenced to room temperature. Resonators experience a large blueshift upon cooling, with the small redshift of (a) only occurring once off-resonant TLSs are no longer thermally populated. (c) Total TLS loss $F\delta_{\mathrm{TLS}}^0$ vs resonator defect width, with error bars indicating one standard deviation.

See the supplementary material for information on device design and fabrication, resonator modeling and loss analysis, and applications to mass sensing.

The authors would like to thank Cyndia Yu, Dale Li, Kevin K. S. Multani, Professor Kent D. Irwin, and Professor Martin Fejer for experimental support and helpful discussions. We acknowledge the support of the David and Lucille Packard Fellowship and the Stanford University Terman Fellowship. This work was funded by the U.S. government through the Office of Naval Research (ONR) under Grant No. N00014-20-1-2422, the U.S. Department of Energy through Grant No. DE-SC0019174, and the National Science Foundation CAREER Award No. ECCS-1941826. E.A.W. was supported by the Department of Defense through the National

Defense & Engineering Graduate Fellowship. Device fabrication was performed at the Stanford Nano Shared Facilities (SNSF), supported by the National Science Foundation under Grant No. ECCS-1542152, and the Stanford Nanofabrication Facility (SNF). The authors wish to thank NTT Research for their financial and technical support.

DATA AVAILABILITY

The data that support the findings of this study are available from the corresponding author upon request.

REFERENCES

[1]A. D. O'Connell, M. Hofheinz, M. Ansmann, R. C. Bialczak, M. Lenander, E. Lucero, M. Neeley, D. Sank, H. Wang, M. Weides, J. Wenner, J. M. Martinis, and A. N. Cleland, Nature **464**, 697 (2010).
[2]P. Arrangoiz-Arriola and A. H. Safavi-Naeini, Phys. Rev. A **94**, 063864 (2016).
[3]Y. Chu, P. Kharel, W. H. Renninger, L. D. Burkhart, L. Frunzio, P. T. Rakich, and R. J. Schoelkopf, Science **358**, 199 (2017).
[4]Y. Chu, P. Kharel, T. Yoon, L. Frunzio, P. T. Rakich, and R. J. Schoelkopf, Nature **563**, 666 (2018).
[5]K. J. Satzinger, Y. P. Zhong, H.-S. Chang, G. A. Peairs, A. Bienfait, M.-H. Chou, A. Y. Cleland, C. R. Conner, É. Dumur, J. Grebel, I. Gutierrez, B. H. November, R. G. Povey, S. J. Whiteley, D. D. Awschalom, D. I. Schuster, and A. N. Cleland, Nature **563**, 661 (2018).
[6]P. Arrangoiz-Arriola, E. A. Wollack, Z. Wang, M. Pechal, W. Jiang, T. P. McKenna, J. D. Witmer, R. Van Laer, and A. H. Safavi-Naeini, Nature **571**, 537 (2019).
[7]L. R. Sletten, B. A. Moores, J. J. Viennot, and K. W. Lehnert, Phys. Rev. X **9**, 021056 (2019).
[8]Y. Chu and S. Gröblacher, Appl. Phys. Lett. **117**, 150503 (2020).
[9]N. Ofek, A. Petrenko, R. Heeres, P. Reinhold, Z. Leghtas, B. Vlastakis, Y. Liu, L. Frunzio, S. M. Girvin, L. Jiang, M. Mirrahimi, M. H. Devoret, and R. J. Schoelkopf, Nature **536**, 441 (2016).
[10]R. Lescanne, M. Villiers, T. Peronnin, A. Sarlette, M. Delbecq, B. Huard, T. Kontos, M. Mirrahimi, and Z. Leghtas, Nat. Phys. **16**, 509 (2020).
[11]W. H. Renninger, P. Kharel, R. O. Behunin, and P. T. Rakich, Nat. Phys. **14**, 601 (2018).
[12]G. S. MacCabe, H. Ren, J. Luo, J. D. Cohen, H. Zhou, A. Sipahigil, M. Mirhosseini, and O. Painter, Science **370**, 840 (2020).
[13]M. Reagor, W. Pfaff, C. Axline, R. W. Heeres, N. Ofek, K. Sliwa, E. Holland, C. Wang, J. Blumoff, K. Chou, M. J. Hatridge, L. Frunzio, M. H. Devoret, L. Jiang, and R. J. Schoelkopf, Phys. Rev. B **94**, 014506 (2016).
[14]A. Megrant, C. Neill, R. Barends, B. Chiaro, Y. Chen, L. Feigl, J. Kelly, E. Lucero, M. Mariantoni, P. J. J. O'Malley, D. Sank, A. Vainsencher, J. Wenner, T. C. White, Y. Yin, J. Zhao, C. J. Palmstrøm, J. M. Martinis, and A. N. Cleland, Appl. Phys. Lett. **100**, 113510 (2012).
[15]M. Pechal, P. Arrangoiz-Arriola, and A. H. Safavi-Naeini, Quantum Sci. Technol. **4**, 015006 (2018).
[16]C. T. Hann, C.-L. Zou, Y. Zhang, Y. Chu, R. J. Schoelkopf, S. M. Girvin, and L. Jiang, Phys. Rev. Lett. **123**, 250501 (2019).
[17]M. Scigliuzzo, L. E. Bruhat, A. Bengtsson, J. J. Burnett, A. F. Roudsari, and P. Delsing, New J. Phys. **22**, 053027 (2020).
[18]N. Kostylev, M. Goryachev, A. D. Bulanov, V. A. Gavva, and M. E. Tobar, Sci. Rep. **7**, 44813 (2017).
[19]P. Arrangoiz-Arriola, E. A. Wollack, M. Pechal, J. D. Witmer, J. T. Hill, and A. H. Safavi-Naeini, Phys. Rev. X **8**, 031007 (2018).
[20]M. S. Khalil, M. J. A. Stoutimore, F. C. Wellstood, and K. D. Osborn, J. Appl. Phys. **111**, 054510 (2012).
[21]C. R. H. McRae, H. Wang, J. Gao, M. Vissers, T. Brecht, A. Dunsworth, D. Pappas, and J. Mutus, arXiv:2006.04718 (2020).
[22]R. N. Patel, C. J. Sarabalis, W. Jiang, J. T. Hill, and A. H. Safavi-Naeini, Phys. Rev. Appl. **8**, 041001 (2017).
[23]W. Liekens, L. Michiels, and A. De Bock, J. Phys. C **4**, 1124 (1971).
[24]W. A. Phillips, Rep. Prog. Phys. **50**, 1657 (1987).
[25]J. Gao, M. Daal, A. Vayonakis, S. Kumar, J. Zmuidzinas, B. Sadoulet, B. A. Mazin, P. K. Day, and H. G. Leduc, Appl. Phys. Lett. **92**, 152505 (2008).
[26]F. Hoehne, Y. A. Pashkin, O. Astafiev, L. Faoro, L. B. Ioffe, Y. Nakamura, and J. S. Tsai, Phys. Rev. B **81**, 184112 (2010).
[27]R. Rivière, S. Deléglise, S. Weis, E. Gavartin, O. Arcizet, A. Schliesser, and T. J. Kippenberg, Phys. Rev. A **83**, 063835 (2011).
[28]J. Suh, A. J. Weinstein, and K. C. Schwab, Appl. Phys. Lett. **103**, 052604 (2013).
[29]B. D. Hauer, P. H. Kim, C. Doolin, F. Souris, and J. P. Davis, Phys. Rev. B **98**, 214303 (2018).
[30]R. Manenti, M. J. Peterer, A. Nersisyan, E. B. Magnusson, A. Patterson, and P. J. Leek, Phys. Rev. B **93**, 041411 (2016).
[31]M. Hamoumi, P. E. Allain, W. Hease, E. Gil-Santos, L. Morgenroth, B. Gérard, A. Lemaître, G. Leo, and I. Favero, Phys. Rev. Lett. **120**, 223601 (2018).
[32]G. Andersson, A. L. O. Bilobran, M. Scigliuzzo, M. M. de Lima, J. H. Cole, and P. Delsing, arXiv:2002.09389 (2020).
[33]R. O. Behunin, F. Intravaia, and P. T. Rakich, Phys. Rev. B **93**, 224110 (2016).
[34]D. C. Mattis and J. Bardeen, Phys. Rev. **111**, 412 (1958).
[35]J. Gao, "The physics of superconducting microwave resonators," Ph.D. thesis (California Institute of Technology, 2008).
[36]J. Zmuidzinas, Annu. Rev. Condens. Matter Phys. **3**, 169 (2012).
[37]T.-S. Kê, Phys. Rev. **71**, 533 (1947).
[38]D. P. Pappas, M. R. Vissers, D. S. Wisbey, J. S. Kline, and J. Gao, IEEE Trans. Appl. Supercond. **21**, 871 (2011).